

Article

# Effect of NaF Doping on the Microstructure and Thermoelectric Performance of BiCuSeO Ceramics

Zhenbing Pei <sup>1</sup>, Guangqi Xiang <sup>1</sup>, Xin Sun <sup>1</sup>, Zhuang Fu <sup>1</sup>, Yanxin Qiao <sup>1</sup> , Lei Wang <sup>1,\*</sup> , Songtao Dong <sup>1,\*</sup>  and Jian Chen <sup>2</sup> 

<sup>1</sup> School of Material Science and Engineering, Jiangsu University of Science and Technology, Zhenjiang 212003, China; zbpei021017@outlook.com (Z.P.); xiaoqi0202@outlook.com (G.X.); 18052685015@163.com (X.S.); yxqiao@just.edu.cn (Y.Q.)

<sup>2</sup> Department of Chemistry, Western University, 1151 Richmond St., London, ON N6A 5B7, Canada; jchen496@uwo.ca

\* Correspondence: wangl\_ray@just.edu.cn (L.W.); stdong@just.edu.cn (S.D.)

**Abstract:** The layered oxyselenide BiCuSeO has attracted significant attention due to its ability to demonstrate low thermal conductivity and a high Seebeck coefficient. This research project involved the synthesis of  $\text{Bi}_{1-x}\text{Na}_x\text{CuSeO}_{1-x}\text{F}_x$  ( $x = 0, 0.05, 0.10, 0.15, \text{ and } 0.20$ ) ceramics using high-energy ball milling and cold isostatic pressing techniques. A comprehensive investigation was conducted to examine the influence of co-doping NaF on the thermoelectric properties of BiCuSeO ceramics. The substitution of  $\text{Bi}^{3+}$  with  $\text{Na}^+$  introduces a substantial number of holes, resulting in a remarkable improvement in the electrical conductivity and power factor. The conductivity was significantly increased from  $9.10 \text{ S cm}^{-1}$  (BiCuSeO) to  $94.5 \text{ S cm}^{-1}$  ( $\text{Bi}_{0.85}\text{Na}_{0.15}\text{CuSeO}_{0.85}\text{F}_{0.15}$ ) at 323 K. Additionally, at 823 K, the power factor of the  $\text{Bi}_{0.85}\text{Na}_{0.15}\text{CuSeO}_{0.85}\text{F}_{0.15}$  sample reached  $44.8 \times 10^{-5} \text{ W/m K}^2$ . Furthermore, the  $\text{Bi}_{1-x}\text{Na}_x\text{CuSeO}_{1-x}\text{F}_x$  ceramics demonstrated a minimum thermal conductivity of  $0.43 \text{ W m}^{-1} \text{ K}^{-1}$ . Consequently, the  $\text{Bi}_{0.85}\text{Na}_{0.15}\text{CuSeO}_{0.85}\text{F}_{0.15}$  sample achieved a maximum ZT value of 0.78, which is 7.09 times higher than that of the pure BiCuSeO sample (0.11).

**Keywords:** high-energy milling; BiCuSeO; thermoelectric performance; microstructure; double doping



**Citation:** Pei, Z.; Xiang, G.; Sun, X.; Fu, Z.; Qiao, Y.; Wang, L.; Dong, S.; Chen, J. Effect of NaF Doping on the Microstructure and Thermoelectric Performance of BiCuSeO Ceramics. *Coatings* **2023**, *13*, 2069. <https://doi.org/10.3390/coatings13122069>

Academic Editor: Csaba Balázsi

Received: 6 November 2023

Revised: 2 December 2023

Accepted: 8 December 2023

Published: 12 December 2023



**Copyright:** © 2023 by the authors. Licensee MDPI, Basel, Switzerland. This article is an open access article distributed under the terms and conditions of the Creative Commons Attribution (CC BY) license (<https://creativecommons.org/licenses/by/4.0/>).

## 1. Introduction

The problems of environmental pollution and energy crisis are rapidly worsening. Currently, in the conventional procedure of utilizing fossil energy, only a small proportion of the mineral energy is converted and utilized, with the majority of the remaining energy being dissipated as heat [1]. Extensive research has been conducted by scientists to explore renewable and ecofriendly energy sources while also improving energy efficiency. Thermoelectric materials exploit the carrier and phonon transmission properties within solid materials to enable the direct conversion between electric energy and heat energy, making them a promising environmentally friendly energy material [1,2]. A dimensionless figure of merit is used to evaluate the thermoelectric properties of materials. This can be calculated using the equation  $ZT = S^2\sigma T/\kappa$ . In this equation,  $S$ ,  $\sigma$ ,  $T$ , and  $\kappa$  represent the Seebeck coefficient, electrical conductivity, absolute temperature, and thermal conductivity, respectively [3–5]. Nonetheless, the interdependence of  $S$ ,  $\sigma$ , and  $\kappa$  presents a challenge in simultaneously optimizing multiple parameters and enhancing thermoelectric performance. [6,7]. The concept of phonon glass electron crystals offers a potential solution to this obstacle [8]. Among them, layered material is an ideal candidate material [9–15]. The BiCuSeO system with low thermal conductivity and a high Seebeck coefficient has garnered significant interest [12–15]. Figure 1a illustrates the layered structure of BiCuSeO, which belongs to the ZrCuSiAs type and is classified under the  $P4/nmm$  space group. The crystal structure comprises a stack of alternating layers in the  $C$ -axis direction. These layers

consist of an insulating layer  $(\text{Bi}_2\text{O}_2)^{2+}$  and a conducting layer  $(\text{Cu}_2\text{Se}_2)^{2-}$ . The  $\text{Bi}_2\text{O}_2$  layer functions as a charge storage layer, comprising a slightly deformed  $\text{Bi}_4\text{O}$  octahedron with shared Bi–Bi edges. Moreover, the  $\text{Cu}_2\text{Se}_2$  layer serves as a carrier transport surface, composed of slightly deformed  $\text{CuSe}_4$  tetrahedra with shared Se–Se sides [16–18]. Additionally, the weak chemical bonding between the two layers and the junction connecting them enhances phonon scattering, resulting in an exceptionally low thermal conductivity ( $0.40 \text{ Wm}^{-1}\text{K}^{-1}$  at 923 K) [13].

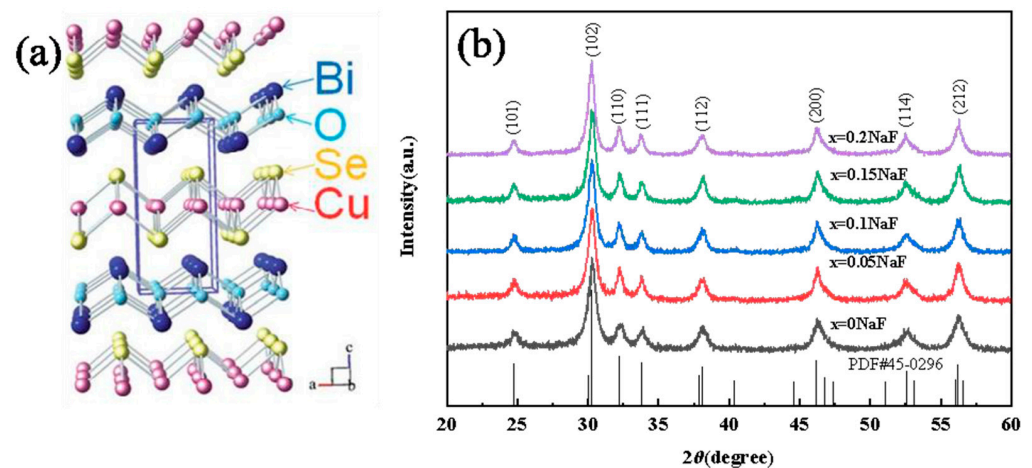


**Figure 1.** (a) Schematic diagram of the crystal structure of  $\text{BiCuSeO}$ ; (b) XRD pattern of  $\text{Bi}_{1-x}\text{Na}_x\text{CuSeO}_{1-x}\text{F}_x$  ( $x = 0, 0.05, 0.10, 0.15,$  and  $0.20$ ) ceramics.

However, the electrical conductivity of  $\text{BiCuSeO}$  is considerably restricted due to its low hole concentration, which hinders the achievement of a high ZT value. To address this issue, the researchers employed techniques such as element doping to enhance the material's conductivity, adjusted the band gap to optimize the carrier concentration, and utilized texturization to increase carrier mobility [19,20]. The improvement of the thermoelectric performance of  $\text{BiCuSeO}$  can be achieved via the doping of monovalent elements ( $\text{Na}^+$ ,  $\text{K}^+$ ,  $\text{Ag}^+$ , etc.) or bivalent elements ( $\text{Mg}^{2+}$ ,  $\text{Ca}^{2+}$ ,  $\text{Ba}^{2+}$ ,  $\text{Pb}^{2+}$ , etc.) at the Bi site or by increasing the concentration of hole carriers using Bi, Cu, and O vacancies and ball milling [14–17,21–23]. Additionally, the technique of dual doping has been identified as an efficient approach to enhancing the thermoelectric performance of materials. By introducing Zn into the Bi and S into the O positions of  $\text{BiCuSeO}$ , Sun et al. successfully improved its ZT value to 0.68 at 750 K [24]. Guang-Kun Ren et al. conducted a study in which they introduced dopants of Pb and Te into the Bi and Se positions, respectively. The substitution of Te at the Se sites had a significant impact on the extent of chemical bonding and the mass of effective carriers. As a result, this led to a weakening of the coupling between the carriers and phonons, ultimately enhancing carrier mobility and resulting in high conductivity [25]. Via the utilization of mechanical alloying, the  $\text{BiCuSeO}$  system achieved a ZT value of 1.08 by incorporating Pb and Ni elements into the Bi and Cu sites [19]. The substitution of Bi elements with Pb and In elements led to the attainment of a ZT value of 1.23 in the  $\text{BiCuSeO}$  system [26]. Liu et al. observed that the incorporation of Pb and Ca elements into the Bi site of  $\text{BiCuSeO}$  not only enhanced the conductivity and thermal conductivity but also increased the effective mass of carriers, thereby preserving a high Seebeck coefficient for the material. Consequently, the doped  $\text{BiCuSeO}$  achieved a ZT value of 1.5 [27], which represents the highest value within the current system.

As demonstrated by the aforementioned results, co-doping of elements can significantly improve the thermoelectric performance of  $\text{BiCuSeO}$ . While there is a substantial amount of research on the Bi, Cu, and Se dopants in  $\text{BiCuSeO}$ , there is a scarcity of information regarding the O dopants. Additionally, studies [14] and [28] have indicated that the ZT values of the  $\text{BiCuSeO}$  system can be enhanced via the doping of F and S elements at the O

site. The majority of the materials are synthesized using the solid-state reaction sintering technique. The drawback of this approach is the lengthy requirement for calcination of the raw materials, whereas the high-energy ball milling technique enables the rapid synthesis of the raw materials. In light of this, the high-energy ball milling technique was employed to swiftly synthesize Na and F co-doped BiCuSeO ceramics. A systematic investigation was conducted to assess the influence of incorporating sodium into the bismuth position and fluorine into the oxygen position on the microstructure and thermoelectric properties of the BiCuSeO.

## 2. Experimental

### 2.1. Synthesis of Starting Material

The  $\text{Bi}_{1-x}\text{Na}_x\text{CuSeO}_{1-x}\text{F}_x$  ( $x = 0, 0.05, 0.10, 0.15, \text{ and } 0.20$ ) ceramics were fabricated using high-energy ball milling and cold isostatic pressing techniques [29,30]. Initially, the mass of the raw material was determined based on the chemical formula of  $\text{Bi}_{1-x}\text{Na}_x\text{CuSeO}_{1-x}\text{F}_x$  ( $x = 0, 0.05, 0.10, 0.15, \text{ and } 0.20$ ).  $\text{Bi}_2\text{O}_3$  (99.999%, Aladdin), Bi (99.999%, Aladdin), Cu (99.999%, Aladdin), Se (99.999%, Aladdin), and NaF (99.99%, Aladdin) were selected. Subsequently, the raw material powder of  $\text{Bi}_{1-x}\text{Na}_x\text{CuSeO}_{1-x}\text{F}_x$  was measured and introduced into a ball mill tank within a high-energy planetary ball mill. The ball mill tank utilized in this study was a 500 mL cemented carbide ball grinding tank, while the ball employed had a diameter of 10 mm and was also made of cemented carbide. The proportion of the ball to material was kept at a ratio of 30 to 1, while the milling speed was adjusted to 560 rpm. A dry ball milling process was employed. The duration of the ball milling process spanned 2 h. To mitigate the potential occurrence of elevated temperatures and subsequent side reactions during the ball milling process, and produced side reactions, a cycle approach consisting of 10 min of ball milling followed by +3 min of cooling was implemented. Following the ball milling process, the powder was placed into an elongated rubber balloon, and shaped into diameters of 10 mm and 15 mm. It was then subjected to a cold isostatic pressing process at a pressure of 300 MPa for 20 min. Subsequently, the resulting rod sample was sealed in a quartz tube (vacuum  $\sim 10^{-3}$  pa) and gradually heated to 450 °C at a rate of 5 °C/min. A 2-h calcination process was then carried out in a Muffle furnace. The utilization of low-temperature sintering effectively mitigates the growth of the ceramic sample's grains. Finally, the sintered sample was prepared into dimensions of 15 mm  $\times$  3 mm  $\times$  3 mm and  $\varnothing$ 12.5 mm  $\times$  2 mm for thermoelectric performance testing.

### 2.2. Characterization

Phase analysis of  $\text{Bi}_{1-x}\text{Na}_x\text{CuSeO}_{1-x}\text{F}_x$  ( $x = 0, 0.05, 0.10, 0.15, \text{ and } 0.20$ ) ceramics was conducted on an X-ray diffractometer (XRD, Bruker D8 Advance, Karlsruhe, Germany). The XRD analysis utilized the Cu  $K_\alpha$  line and encompassed a scanning range of 20° to 60° at a scanning speed of 4°/min and a voltage of 40 kV and 40 mA. The fracture morphology of the ceramics was analyzed using field emission scanning electron microscopy (FESEM; Merlin Compact, Carl Zeiss, Oberkochen, Germany). X-ray photoelectron spectroscopy (XPS) was employed to analyze the valence states of the samples.  $S$  and  $\sigma$  were concurrently measured using a ZEM-3 thermoelectric performance tester using standard DC four-probe techniques. The  $\kappa$  was determined using the equation  $\kappa = \rho DC_p$ , where  $\rho$  represents the volumetric density determined via the Archimedes method,  $D$  denotes the thermal diffusivity measured using a laser flash apparatus (LFA 457, Netzsch, Selb, Germany), and  $C_p$  signifies the specific heat obtained using a differential scanning calorimetry thermal analyzer (DSC 8000, PerkinElmer, Waltham, MA, USA). The Hall coefficient ( $R_H$ ) was obtained using a Physical Property Measurement System (PPMS, Quantum Corporation, San Diego, CA, USA). The carrier concentration was stimulated using the single-electron approximation ( $R_H = \frac{1}{n \cdot e}$ ,  $R_H$ ,  $n$ , and  $e$  represent the Hall coefficient, carrier concentration, and electron charge, respectively).

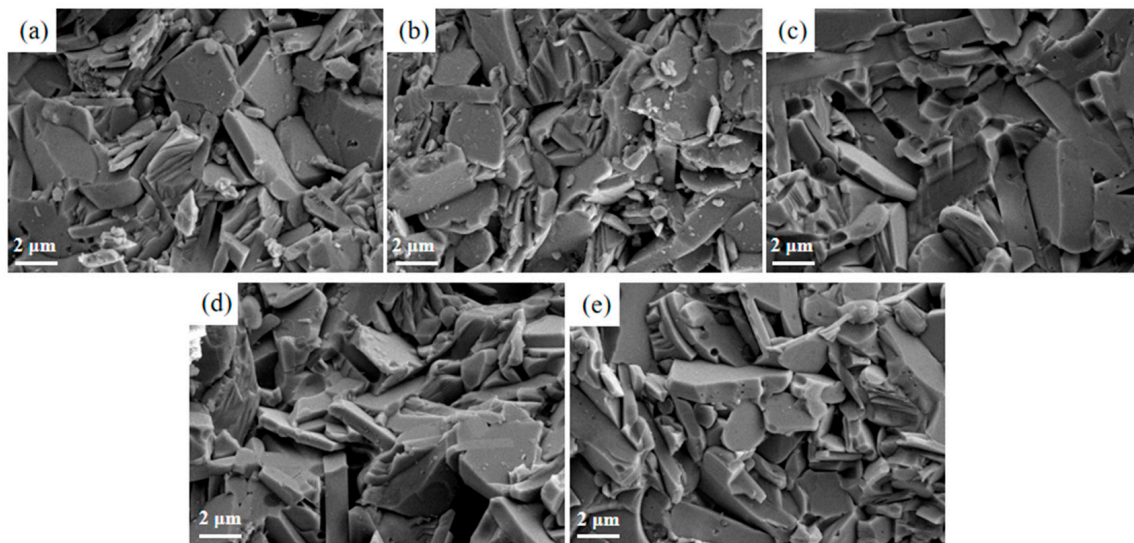
### 3. Results and Discussion

Figure 1b illustrates the XRD patterns of  $\text{Bi}_{1-x}\text{Na}_x\text{CuSeO}_{1-x}\text{F}_x$  ( $x = 0, 0.05, 0.10, 0.15,$  and  $0.20$ ) ceramics. Compared to the standard card of  $\text{BiCuSeO}$  (PDF#45–0296), the diffraction peak position of the  $\text{Bi}_{1-x}\text{Na}_x\text{CuSeO}_{1-x}\text{F}_x$  is found to be consistent with that of the standard card. The obtained results indicate that the synthesized  $\text{Bi}_{1-x}\text{Na}_x\text{CuSeO}_{1-x}\text{F}_x$  ceramics exhibit a single phase. With an increase in the NaF doping amount, the XRD peak of the  $\text{Bi}_{1-x}\text{Na}_x\text{CuSeO}_{1-x}\text{F}_x$  ceramics demonstrates a slight rightward shift. This shift can be attributed to the marginally smaller ionic radius of  $\text{Na}^+$  (0.102 nm) in comparison to  $\text{Bi}^{3+}$  (0.103 nm), as well as the smaller ionic radius of  $\text{F}^-$  (0.133 nm) compared to  $\text{O}^{2-}$  (0.140 nm). This makes the crystal plane spacing smaller. The crystal face spacing and the lattice constants are calculated using the Bragg Equations (1) and (2):

$$\lambda = 2d_{hkl}\sin\theta_{hkl} \quad (1)$$

$$\frac{1}{d^2} = \frac{h^2 + k^2}{a^2} + \frac{l^2}{c^2} \quad (2)$$

where  $d$ ,  $a$ , and  $c$  represent the crystal plane spacing and lattice parameters, correspondingly. Table 1 displays the lattice constants  $a$  and  $c$  of  $\text{Bi}_{1-x}\text{Na}_x\text{CuSeO}_{1-x}\text{F}_x$  ( $x = 0, 0.05, 0.10, 0.15,$  and  $0.20$ ) ceramics. The results indicate that the lattice constant  $a$  of the doped samples increases, while the lattice constant  $c$  decreases with an increase in the NaF doping amount. The crystal face spacing of the  $\text{Bi}_{1-x}\text{Na}_x\text{CuSeO}_{1-x}\text{F}_x$  ceramics is calculated using Equation (2), revealing a negligible change in the crystal face spacing. Consequently, the diffraction peak of the  $\text{Bi}_{1-x}\text{Na}_x\text{CuSeO}_{1-x}\text{F}_x$  ceramics does not exhibit any noticeable deviation. Table 1 shows the computation of the grain size for  $\text{Bi}_{1-x}\text{Na}_x\text{CuSeO}_{1-x}\text{F}_x$  ceramics utilizing the Debye–Scherrer formula  $D_c = 0.89\lambda / (B\cos\theta)$ , where  $B$  represents the half-peak width and  $\theta$  signifies the Bragg diffraction angle. The results indicate that the mean grain sizes of  $\text{Bi}_{1-x}\text{Na}_x\text{CuSeO}_{1-x}\text{F}_x$  ( $x = 0, 0.05, 0.10, 0.15,$  and  $0.20$ ) ceramics are 1.92  $\mu\text{m}$ , 1.63  $\mu\text{m}$ , 1.66  $\mu\text{m}$ , 1.68  $\mu\text{m}$ , and 1.72  $\mu\text{m}$ , respectively. The fracture morphology of  $\text{Bi}_{1-x}\text{Na}_x\text{CuSeO}_{1-x}\text{F}_x$  ( $x = 0, 0.05, 0.10, 0.15,$  and  $0.20$ ) ceramics is depicted in Figure 2, demonstrating the presence of layered structures, good crystallinity, and a void-free surface. Based on Figure 2, the  $\text{Bi}_{1-x}\text{Na}_x\text{CuSeO}_{1-x}\text{F}_x$  ceramics exhibit tightly stacked grains, with an average grain size of approximately 2  $\mu\text{m}$  and minimal variation. These results align with the results obtained in calculations using the Scherrer formula.



**Figure 2.** Fracture morphology of  $\text{Bi}_{1-x}\text{Na}_x\text{CuSeO}_{1-x}\text{F}_x$  ( $x = 0, 0.05, 0.10, 0.15,$  and  $0.20$ ) ceramics, (a)  $x=0$ , (b)  $x=0.05$ , (c)  $x=0.10$ , (d)  $x=0.15$ , (e)  $x=0.20$ .

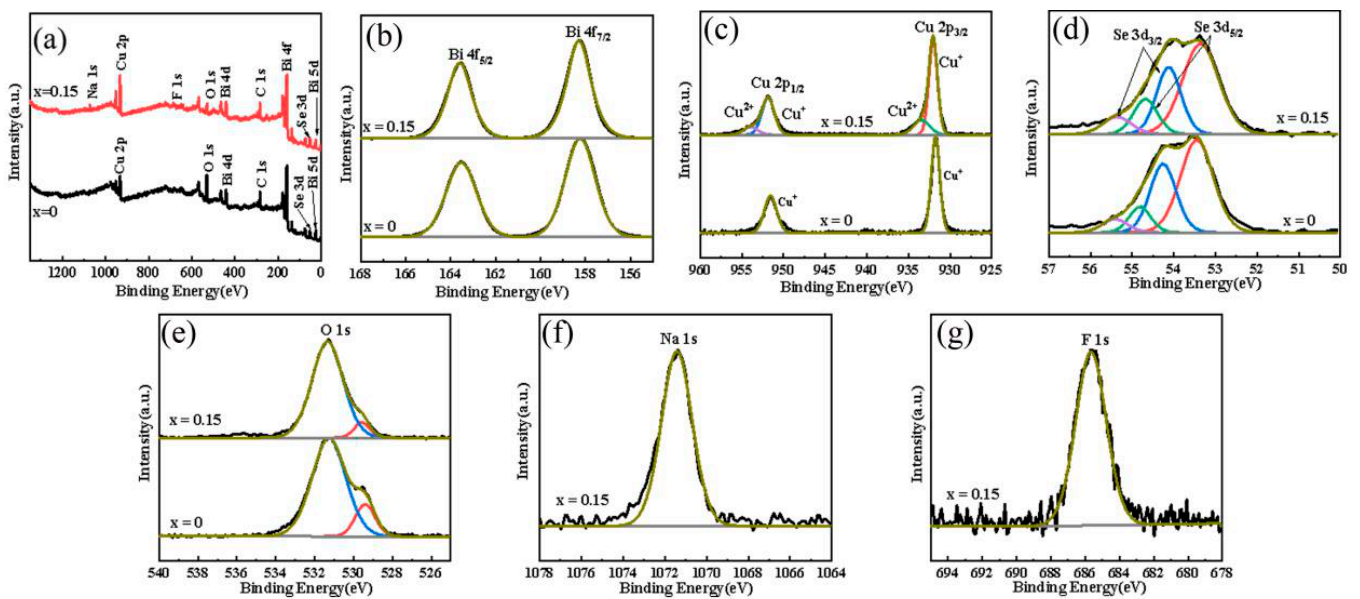
**Table 1.** Lattice parameters and grain sizes of  $\text{Bi}_{1-x}\text{Na}_x\text{CuSeO}_{1-x}\text{F}_x$  ( $x = 0, 0.05, 0.10, 0.15,$  and  $0.20$ ).

Samples	$a(\text{\AA})$	$c(\text{\AA})$	Grain Size ( $\mu\text{m}$ )
$x = 0$	3.93908	8.90968	1.92
$x = 0.05$	3.92563	8.92035	1.63
$x = 0.10$	3.91786	8.92214	1.66
$x = 0.15$	3.91661	8.93309	1.68
$x = 0.20$	3.92251	8.93120	1.72

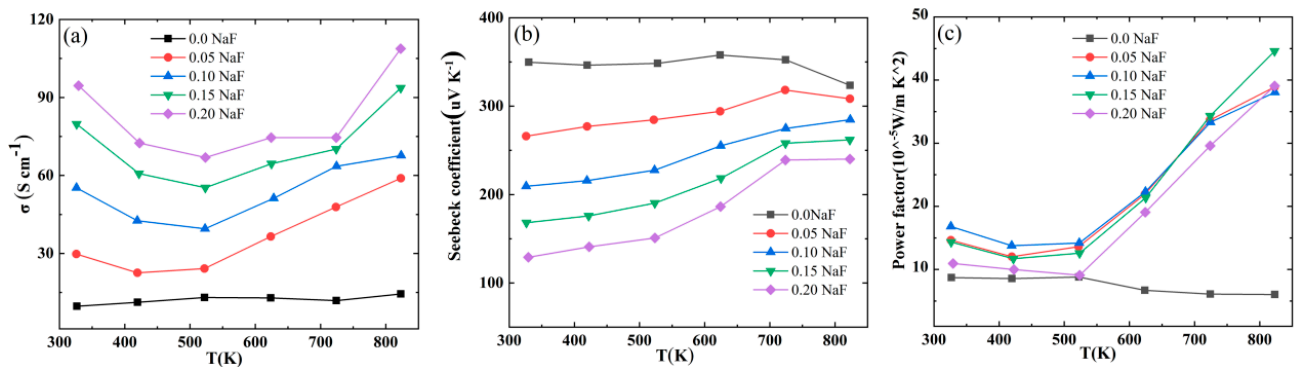
The full XPS spectrum of the  $\text{Bi}_{1-x}\text{Na}_x\text{CuSeO}_{1-x}\text{F}_x$  ( $x = 0, 0.15$ ) ceramics are displayed in Figure 3a. The spectrum reveals the presence of Bi, Cu, Se, and O elements in the undoped sample, while the doped NaF sample contains Bi, Cu, Se, O, Na, and F elements. Combined with the XRD results, it is possible to verify the successful integration of Na and F elements into the BiCuSeO system. Figure 3b–f show the XPS high-resolution spectra of bismuth (Bi), copper (Cu), selenium (Se), oxygen (O), and sodium (Na) in the  $\text{Bi}_{1-x}\text{Na}_x\text{CuSeO}_{1-x}\text{F}_x$  ( $x = 0, 0.15$ ) ceramics. The high-resolution spectrum of Bi 4f in Figure 3b demonstrate the presence of two spin–orbit peaks, corresponding to the spin–orbit peak of Bi 4f<sub>7/2</sub> and the spin–orbit peak of Bi 4f<sub>5/2</sub>, respectively. The presence of two distinct peaks at 158.28 eV and 163.58 eV, exhibiting a disparity of 5.3 eV, implies the existence of Bi atoms in the Bi<sup>3+</sup> state [23,31,32]. In Figure 3c, the 2p orbits of Cu elements in the pure BiCuSeO sample exhibit a split into two distinct peaks, namely the spin–orbit peak of Cu 2p<sub>3/2</sub> at 931.68 eV and the spin–orbit peak of Cu 2p<sub>1/2</sub> at 951.58 eV. This difference of 19.9 eV indicates the presence of Cu<sup>+</sup> ions in the sample. The spin–orbit splitting of Cu 2p in the  $\text{Bi}_{0.85}\text{Na}_{0.15}\text{CuSeO}_{0.85}\text{F}_{0.15}$  sample is observed to be divided into four peaks. Based on the results, the presence of Cu<sup>2+</sup> in the  $\text{Bi}_{0.85}\text{Na}_{0.15}\text{CuSeO}_{0.85}\text{F}_{0.15}$  compound is consistent with the previous literature [32]. The Se 3d high-resolution spectrum, as depicted in Figure 3d, reveals a complex spin–orbit splitting pattern. Specifically, the spin–orbit peaks of Se 3d<sub>5/2</sub> are observed at 53.48 eV and 54.88 eV, while the spin–orbit peaks of Se 3d<sub>3/2</sub> are detected at 54.28 eV and 55.48 eV. The indication of Se atoms in the form of Se<sup>2−</sup> is derived from the low binding energy observed in the Se 3d<sub>5/2</sub> and Se 3d<sub>3/2</sub> spin–orbit peaks, which aligns with the results documented in the literature [32]. Furthermore, the high binding energy observed in the spin–orbit peaks suggests an interaction between the layers of Se. In Figure 3e, the high-resolution spectrum of O 1s displays two spin–orbit peaks. The peak at 529.4 eV corresponds to the lattice oxygen, while the high binding energy peak indicates the presence of an oxygen vacancy. To determine the alteration in oxygen content between the two types, the ratio of the areas of the two peaks is utilized. The BiCuSeO sample exhibits an area ratio of 0.2 for lattice oxygen to oxygen vacancy, whereas the  $\text{Bi}_{0.85}\text{Na}_{0.15}\text{CuSeO}_{0.85}\text{F}_{0.15}$  displays an area ratio of 0.09. These results indicate that the introduction of NaF as a dopant increases the presence of lattice defect in the  $\text{Bi}_{1-x}\text{Na}_x\text{CuSeO}_{1-x}\text{F}_x$  sample, which aligns with previous literature reports [33,34]. Figure 3f depicts the high-resolution spectrum of Na 1s in the  $\text{Bi}_{0.85}\text{Na}_{0.15}\text{CuSeO}_{0.85}\text{F}_{0.15}$  sample, wherein the Na 1s orbital manifests a solitary peak, indicating the presence of Na with a +1 valence, which aligns with the results documented in the literature [35]. Similarly, the 1s spin–orbit peak of F in Figure 3g confirms the existence of F<sup>−</sup> in a manner that aligns with the outcomes reported in the literature [36].

Figure 4a illustrates the electrical conductivity ( $\sigma$ ) as a function of temperature for the  $\text{Bi}_{1-x}\text{Na}_x\text{CuSeO}_{1-x}\text{F}_x$  ( $x = 0, 0.05, 0.10, 0.15,$  and  $0.20$ ) ceramics. In the case of the pure BiCuSeO sample, the conductivity remains consistently low across the entire range of test temperatures. However, upon the introduction of doping, a significant improvement in conductivity is observed. The  $\sigma$  of  $\text{Bi}_{1-x}\text{Na}_x\text{CuSeO}_{1-x}\text{F}_x$  ceramics demonstrates a positive correlation with the level of NaF doping across the entire temperature range. Specifically, at 323 K, the conductivity increases from 9.10 S cm<sup>−1</sup> (BiCuSeO) to 94.50 S cm<sup>−1</sup> ( $\text{Bi}_{0.80}\text{Na}_{0.20}\text{CuSeO}_{0.80}\text{F}_{0.20}$ ), resulting in a remarkable increase of 900%. The primary factor contributing to the increased conductivity of  $\text{Bi}_{1-x}\text{Na}_x\text{CuSeO}_{1-x}\text{F}_x$  ( $x = 0, 0.05, 0.10, 0.15,$  and  $0.20$ ) ceramics is the rise in carrier concentration within the system, calculated using

the equation: the relationship between conductivity ( $\sigma$ ) and carrier concentration ( $n$ ) and mobility ( $\mu$ ) can be represented as  $\sigma = en\mu$ , where  $e$  represents the charge of an electron. The carrier concentration is determined using the expression  $n = 1/eR_H$ . Table 2 demonstrates the carrier concentration and mobility values for  $\text{Bi}_{1-x}\text{Na}_x\text{CuSeO}_{1-x}\text{F}_x$  ( $x = 0, 0.05, 0.10, 0.15,$  and  $0.20$ ) ceramics. With the introduction of NaF, the electrical conductivity  $\sigma$  experiences an initial decrease, followed by an increase as temperature rises, ultimately reaching a critical point at 523 K. Within the temperature range spanning from 323 K to 523 K, the conductivity of the ceramics doped with NaF diminishes with an increasing temperature, demonstrating the characteristics of a degenerate semiconductor. However, as the temperature surpasses 523 K, the conductivity of the sample exhibits a proportional increase with the temperature. This behavior indicates that the sample exhibits semiconductor properties that are non-degenerate, attributable to its intrinsic excitation. The conductivity of  $\text{Bi}_{0.80}\text{Na}_{0.20}\text{CuSeO}_{0.80}\text{F}_{0.20}$  reaches a maximum of  $108.6 \text{ S cm}^{-1}$  at 823 K.



**Figure 3.** (a) Full spectrum of  $\text{Bi}_{1-x}\text{Na}_x\text{CuSeO}_{1-x}\text{F}_x$  ( $x = 0, 0.15$ ) ceramics, (b) Bi 4f, (c) Cu 2p, (d) Se 3d, (e) O 1s, (f) Na 1s, (g) F 1s high-resolution spectrum.



**Figure 4.** (a) Electrical conductivity, (b) Seebeck coefficient  $S$ , and (c) PF as a function of temperature for  $\text{Bi}_{1-x}\text{Na}_x\text{CuSeO}_{1-x}\text{F}_x$  ( $x = 0, 0.05, 0.10, 0.15,$  and  $0.20$ ) ceramics.

**Table 2.** Carrier concentration, mobility, effective mass, and density of  $\text{Bi}_{1-x}\text{Na}_x\text{CuSeO}_{1-x}\text{F}_x$  ( $x = 0, 0.05, 0.10, 0.15,$  and  $0.20$ ) ceramics at room temperature.

Samples	$n$ ( $10^{19} \text{ cm}^{-3}$ )	$\mu$ ( $\text{cm}^2 \text{ V}^{-1} \text{ S}^{-1}$ )	$m^*$ ( $m_0$ )	$\rho$ ( $\text{g/cm}^3$ )
$x = 0$	0.99	6.109	0.7621	7.517
$x = 0.05$	7.54	2.466	2.1792	7.495
$x = 0.10$	10.3	3.352	2.1016	7.473
$x = 0.15$	51.5	0.969	4.9396	7.444
$x = 0.20$	57.8	1.022	4.0589	7.367

Figure 4b illustrates the temperature-dependent  $S$  of the  $\text{Bi}_{1-x}\text{Na}_x\text{CuSeO}_{1-x}\text{F}_x$  ( $x = 0, 0.05, 0.10, 0.15,$  and  $0.20$ ) ceramics. The positive signs of all Seebeck coefficients indicate that the  $\text{Bi}_{1-x}\text{Na}_x\text{CuSeO}_{1-x}\text{F}_x$  ceramic functions as a P-type semiconductor with predominantly hole charge carriers. The Seebeck coefficient of  $\text{BiCuSeO}$  exhibits a value of  $349 \mu\text{V K}^{-1}$  at 323 K, while it decreases to  $324 \mu\text{V K}^{-1}$  at 823 K. Moreover, the Seebeck coefficient of the  $\text{Bi}_{1-x}\text{Na}_x\text{CuSeO}_{1-x}\text{F}_x$  samples decreases as the NaF doping content increases at 323 K. In the context of degenerate semiconductors, employing a parabolic band structure and adopting the phonon scattering approximation, the Pisarenko relationship can offer an approximate depiction of  $S$  [37,38].

$$S = \frac{8\pi^2 k_B^2 T}{3eh^2} m^* \left( \frac{\pi}{3n} \right)^{2/3} \quad (3)$$

This relationship encompasses various parameters, including the Seebeck coefficient ( $S$ ), Boltzmann constant ( $k_B$ ), absolute temperature ( $T$ ), carrier charge ( $e$ ), reduced Planck constant ( $h$ ), carrier effective mass ( $m^*$ ), and carrier concentration ( $n$ ). By examining Formula (3), it becomes evident that the Seebeck coefficient exhibits an inverse relationship with the carrier concentration and a direct relationship with the effective mass. The effective mass  $m^*$  can be calculated using Formula (3), as presented in Table 2. It is observed that the effective mass  $m^*$  exhibits an increasing trend as the NaF doping content increases, ranging from  $0.7621 m_0$  in the pure sample to  $4.9396 m_0$  in the  $\text{Bi}_{0.85}\text{Na}_{0.15}\text{CuSeO}_{0.85}\text{F}_{0.15}$  sample. These results indicate that the decrease in the Seebeck coefficient of  $\text{Bi}_{1-x}\text{Na}_x\text{CuSeO}_{1-x}\text{F}_x$  ceramics primarily stems from the concurrent increase in the carrier concentration within the system.

The curves of the power factor as a function of temperature are shown in Figure 4c, illustrating that the PF of all doped samples exceeds that of pure  $\text{BiCuSeO}$  across the entire temperature range due to a significant increase in conductivity. Notably, the  $\text{Bi}_{0.90}\text{Na}_{0.10}\text{CuSeO}_{0.90}\text{F}_{0.10}$  samples exhibit the highest power factor, reaching  $16.7 \times 10^{-5} \text{ W/m K}^{-2}$  at 323 K. Furthermore, as the temperature increases, the power factor of the  $\text{Bi}_{0.85}\text{Na}_{0.15}\text{CuSeO}_{0.85}\text{F}_{0.15}$  samples gradually surpasses that of the  $\text{Bi}_{0.90}\text{Na}_{0.10}\text{CuSeO}_{0.90}\text{F}_{0.10}$  samples. At 823 K, the  $\text{Bi}_{0.85}\text{Na}_{0.15}\text{CuSeO}_{0.85}\text{F}_{0.15}$  sample demonstrates a maximum PF of  $44.8 \times 10^{-5} \text{ W/m K}^2$ , which is approximately 7.11 times greater than that of the pure  $\text{BiCuSeO}$  sample ( $6.3 \times 10^{-5} \text{ W/mK}^2$ ).

Figure 5a displays the relationship between the thermal conductivity ( $\kappa$ ) and temperature for  $\text{Bi}_{1-x}\text{Na}_x\text{CuSeO}_{1-x}\text{F}_x$  ( $x = 0, 0.05, 0.10, 0.15,$  and  $0.20$ ) ceramics. The thermal conductivity  $\kappa$  of  $\text{BiCuSeO}$  experiences a significant decrease from  $0.98 \text{ Wm}^{-1} \text{ K}^{-1}$  at 323 K to  $0.43 \text{ Wm}^{-1} \text{ K}^{-1}$  at 823 K, while the thermal conductivity remains virtually unchanged even after the introduction of NaF doping. Typically, the total thermal conductivity comprises two components: the electron thermal conductivity  $\kappa_e$  and the lattice thermal conductivity  $\kappa_l$ . The calculation of the electron thermal conductivity often involves the utilization of the Wiedemann–Franz relationship ( $\kappa_e = L\sigma T$ ), where  $\sigma$  represents the electrical conductivity,  $T$  denotes the absolute temperature, and  $L$  signifies the Lorentz constant.  $L$  can be determined using the formula  $L = 1.5 + \exp\left(\frac{-|S|}{116}\right)$  [39], with the Sommerfeld value ( $L_0$ ) being equal to  $2.44 \times 10^{-8} \text{ W } \Omega \text{ K}^{-2}$ . Figure 5b illustrates the temperature dependence of the electron thermal conductance in  $\text{Bi}_{1-x}\text{Na}_x\text{CuSeO}_{1-x}\text{F}_x$  ( $x = 0, 0.05, 0.10,$

0.15, and 0.20) ceramics. The figure demonstrates an increasing trend in the electron thermal conductivity of the  $\text{Bi}_{1-x}\text{Na}_x\text{CuSeO}_{1-x}\text{F}_x$  ceramics as the level of doping increases. This can be primarily attributed to the corresponding increase in electrical conductivity. Notably, the  $\text{Bi}_{0.8}\text{Na}_{0.2}\text{CuSeO}_{0.8}\text{F}_{0.2}$  ceramics exhibit a maximum electron thermal conductivity of  $0.219 \text{ W m}^{-1} \text{ K}^{-1}$  at 823 K. The results indicate that the lattice thermal conductivity plays a dominant role in the BiCuSeO system.

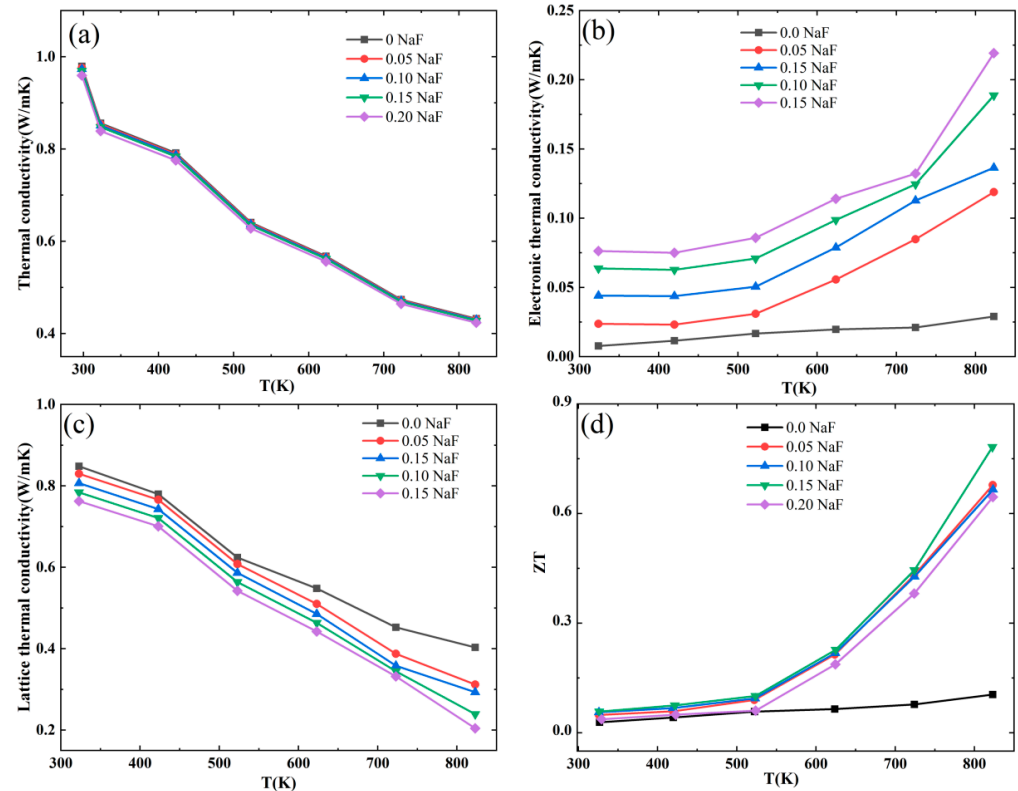


**Figure 5.** The relationship between temperature and (a) total thermal conductivity  $\kappa$ , (b) electronic thermal conductivity  $\kappa_e$ , (c) lattice thermal conductivity  $\kappa_l$ , (d) ZT value of  $\text{Bi}_{1-x}\text{Na}_x\text{CuSeO}_{1-x}\text{F}_x$  ( $x = 0, 0.05, 0.10, 0.15,$  and  $0.20$ ) ceramics.

The relationship between the lattice thermal conductivity and temperature for the  $\text{Bi}_{1-x}\text{Na}_x\text{CuSeO}_{1-x}\text{F}_x$  ( $x = 0, 0.05, 0.10, 0.15,$  and  $0.20$ ) ceramics is depicted in Figure 5c. As the temperature increases, the lattice thermal conductivity of the  $\text{Bi}_{1-x}\text{Na}_x\text{CuSeO}_{1-x}\text{F}_x$  samples decreases. This phenomenon can be attributed to the strengthening of lattice vibration and the increased scattering ability of phonons, resulting in a reduction in the lattice thermal conductivity as the temperature increases. In comparison to the pure BiCuSeO sample, the decrease in the lattice thermal conductivity of  $\text{Bi}_{1-x}\text{Na}_x\text{CuSeO}_{1-x}\text{F}_x$  ceramics is primarily caused by the decrease in grain size induced by the NaF doping. Table 1 presents that the grain sizes of  $\text{Bi}_{1-x}\text{Na}_x\text{CuSeO}_{1-x}\text{F}_x$  ( $x = 0, 0.05, 0.10, 0.15,$  and  $0.20$ ) ceramics are  $1.92 \mu\text{m}$ ,  $1.63 \mu\text{m}$ ,  $1.66 \mu\text{m}$ ,  $1.68 \mu\text{m}$ , and  $1.72 \mu\text{m}$ , respectively. It is observed that the grain sizes of the doped samples are comparatively smaller than those of the pure BiCuSeO sample, resulting in an enhanced ability to scatter phonons. Consequently, the lattice thermal conductivity of  $\text{Bi}_{1-x}\text{Na}_x\text{CuSeO}_{1-x}\text{F}_x$  ceramics, when doped with NaF, decreases with an increase in the doping amount.

Figure 5d illustrates the temperature-dependent ZT values for  $\text{Bi}_{1-x}\text{Na}_x\text{CuSeO}_{1-x}\text{F}_x$  ( $x = 0, 0.05, 0.10, 0.15,$  and  $0.20$ ) ceramics. The ZT value of  $\text{Bi}_{1-x}\text{Na}_x\text{CuSeO}_{1-x}\text{F}_x$  ceramics is primarily determined by its power factor, as the variation in thermal conductivity is insignificant. The figure illustrates that the ZT value exhibits a positive correlation with the test temperature. Specifically,  $\text{Bi}_{0.85}\text{Na}_{0.15}\text{CuSeO}_{0.85}\text{F}_{0.15}$  achieves a peak ZT value of 0.78 at 823 K, which is 7.09 times greater than that of pure BiCuSeO. The results indicate that a

significant improvement in the thermoelectric performance of BiCuSeO is observed with the addition of NaF.

#### 4. Conclusions

In this study, the synthesis of NaF-doped BiCuSeO was successfully achieved by employing high-energy ball milling and cold isostatic pressing techniques. The incorporation of Na and F elements led to a reduction in the grain size of the  $\text{Bi}_{1-x}\text{Na}_x\text{CuSeO}_{1-x}\text{F}_x$  samples, an elevation in the carrier concentration, and consequently an enhancement in the electrical conductivity. At 823 K, the power factor of the pristine sample increases from  $6.3 \times 10^{-5} \text{ W/m K}^2$  to  $44.8 \times 10^{-5} \text{ W/mK}^2$  in the  $\text{Bi}_{0.85}\text{Na}_{0.15}\text{CuSeO}_{0.85}\text{F}_{0.15}$  sample. The reduction in grain size in the doped samples enhances the phonon scattering capability of the system, thereby leading to a decrease in the lattice thermal conductivity. Specifically, the  $\text{Bi}_{0.85}\text{Na}_{0.15}\text{CuSeO}_{0.85}\text{F}_{0.15}$  sample attains a maximum ZT value of 0.78 at 823 K, demonstrating a 7.09-fold improvement (0.11) compared to the original BiCuSeO sample. The above results indicate that co-doping is an successful effective strategy for enhancing the thermoelectric performance of the materials.

**Author Contributions:** Investigation, Z.P.; methodology, G.X.; formal analysis, X.S. and J.C.; conceptualization, Z.F.; data curation, Y.Q.; writing—original draft preparation, L.W.; writing—review and editing, S.D. All authors have read and agreed to the published version of the manuscript.

**Funding:** This research was funded by the National Natural Science Foundation of China (grant number 51702132).

**Institutional Review Board Statement:** Not applicable.

**Informed Consent Statement:** Not applicable.

**Data Availability Statement:** Data is contained within the article.

**Acknowledgments:** Songtao Dong expresses gratitude for the opportunity provided by the open project of the National Laboratory of Solid-State Microstructures, Nanjing University.

**Conflicts of Interest:** The authors declare no conflict of interest.

#### References

1. Zheng, X.F.; Liu, C.X.; Yan, Y.Y.; Wang, Q. A review of thermoelectrics research—Recent developments and potentials for sustainable and renewable energy applications. *Renew. Sustain. Energy Rev.* **2014**, *32*, 486–503. [[CrossRef](#)]
2. Shi, X.L.; Zou, J.; Chen, Z.G. Advanced Thermoelectric Design: From Materials and Structures to Devices. *Chem. Rev.* **2020**, *120*, 7399–7515. [[CrossRef](#)] [[PubMed](#)]
3. Dong, S.T.; Yu, M.C.; Fu, Z.; Lv, Y.Y.; Yao, S.H.; Chen, Y.B. High thermoelectric performance of NaF-doped  $\text{Bi}_2\text{Ca}_2\text{Co}_2\text{O}_y$  ceramic samples. *J. Mater. Res. Technol.* **2022**, *17*, 1598–1604. [[CrossRef](#)]
4. Fu, Z.; Jiang, J.L.; Dong, S.T.; Yu, M.C.; Zhao, L.J.; Wang, L.; Yao, S.H. Effects of Zr substitution on structure and thermoelectric performance of  $\text{Bi}_2\text{O}_2\text{Se}$ . *J. Mater. Res. Technol.* **2022**, *21*, 640–647. [[CrossRef](#)]
5. Jiang, J.L.; Dong, S.T.; Fu, Z.; Yu, M.C.; Zhao, L.J.; Wang, L. Effect of Ta Doping on the Microstructure and Thermoelectric performance of  $\text{Bi}_2\text{O}_2\text{Se}$ . *Metals* **2022**, *12*, 1881. [[CrossRef](#)]
6. Mori, T. Novel principles and nanostructuring methods for enhanced thermoelectrics. *Small* **2017**, *13*, 1702013. [[CrossRef](#)] [[PubMed](#)]
7. He, J.; Tritt, T.M. Advances in thermoelectric materials research: Looking back and moving forward. *Science* **2017**, *357*, eaak9997. [[CrossRef](#)]
8. Slack, G.A.; Rowe, D. *CRC Handbook of Thermoelectrics*; CRC Press: Boca Raton, FL, USA, 1995.
9. Li, L.; Qiao, Y.X.; Zhang, L.M.; Li, C.T.; Liu, Z.; Ma, R.Y.; Yang, L.L.; Li, J.Y.; Zheng, Y.G. Effect of cavitation erosion induced surface damage on the corrosion behavior of TA31 titanium alloy. *Ultrason. Sonochem.* **2023**, *98*, 106498. [[CrossRef](#)]
10. Huang, M.; Ruof, R.S. Growth of Single-Layer and Multilayer Graphene on Cu/Ni Alloy Substrates. *Acc. Chem. Res.* **2020**, *53*, 800–811. [[CrossRef](#)]
11. Afzal, A.M.; Khan, M.F.; Nazir, G.; Dastgeer, G.; Aftab, S.; Akhtar, I.; Seo, Y.; Eom, J. Gate Modulation of the Spin-orbit Interaction in Bilayer Graphene Encapsulated by  $\text{WS}_2$  flms. *Sci. Rep.* **2018**, *8*, 3412. [[CrossRef](#)]

12. Wang, Z.B.; Zhao, H.; Luo, X.Y.; Han, W.Y.; Wang, H.; Meng, L.H.; She, X.Q.; Quan, A.L.; Peng, Y.X.; Cai, G.J.; et al. Study on the Targeted Improvement Mechanism of the Carrier Concentration and Mobility of BiCuSeO Ceramics. *Micromachines* **2023**, *14*, 1757. [[CrossRef](#)] [[PubMed](#)]
13. Liu, Y.; Zhao, L.D.; Liu, Y.C.; Lin, J.L.; Xu, W. Remarkable enhancement in thermoelectric performance of BiCuSeO by Cu deficiencies. *J. Am. Chem. Soc.* **2011**, *133*, 20112–20115. [[CrossRef](#)] [[PubMed](#)]
14. Li, F.; Wei, T.R.; Kang, F.Y.; Li, J.F. Enhanced thermoelectric performance of Ca-doped BiCuSeO in a wide temperature range. *J. Mater. Chem. A* **2013**, *1*, 11942–11949. [[CrossRef](#)]
15. Ren, G.K.; Lan, J.L.; Butt, S.; Ventura, K.J.; Lin, Y.H.; Nan, C.W. Enhanced thermoelectric performance in Pb-doped BiCuSeO oxyselenides prepared by ultrafast synthesis. *RSC Adv.* **2015**, *5*, 69878–69885. [[CrossRef](#)]
16. Li, J.; Sui, J.; Barreateau, C.; Berardan, D.; Dragoe, N.; Cai, W.; Pei, Y.; Zhao, L.D. Thermoelectric performance of Mg doped p-type BiCuSeO oxyselenides. *J. Alloys Compd.* **2013**, *551*, 649–653. [[CrossRef](#)]
17. Jing, L.; Sui, J.; Barreateau, C.; Berardan, D.; Dragoe, N.; Wei, C.; He, J.; Zhao, L.D. A high thermoelectric figure of merit  $ZT > 1$  in Ba heavily doped BiCuSeO oxyselenides. *Energy Environ. Sci.* **2012**, *5*, 8543–8547.
18. Li, J.; Sui, J.; Pei, Y.; Meng, X.; Berardan, D.; Dragoe, N.; Caia, W.; Zhao, L.D. The roles of Na doping in BiCuSeO oxyselenides as a thermoelectric material. *J. Mater. Chem. A* **2014**, *2*, 4903–4906. [[CrossRef](#)]
19. Feng, B.; Li, G.; Pan, Z.; Hu, X.; Liu, P.; He, Z.; Li, Y.; Fan, X. Enhanced thermoelectric performance in BiCuSeO ceramics by Pb/Ni dual doping and 3D modulation doping. *J. Solid State Chem.* **2019**, *271*, 1–7. [[CrossRef](#)]
20. Park, K.; Kim, D.H.; Hong, H.Y.; Jung, G.W.; Pi, J.W. Influence of Ba<sup>2+</sup> doping on the thermoelectric performance of BiCuSeO fabricated by spark plasma sintering. *Ceram. Int.* **2019**, *45*, 9604–9610. [[CrossRef](#)]
21. Zhao, L.D.; Berardan, D.; Pei, Y.L.; Byl, C.; Dragoe, N. Bi<sub>1-x</sub>Sr<sub>x</sub>CuSeO oxyselenides as promising thermoelectric materials. *Appl. Phys. Lett.* **2010**, *97*, 092118. [[CrossRef](#)]
22. Lan, J.-L.; Ma, W.; Deng, C.; Ren, G.-K.; Lin, Y.-H. High thermoelectric performance of Bi<sub>1-x</sub>K<sub>x</sub>CuSeO prepared by combustion synthesis. *J. Mater. Sci.* **2017**, *52*, 11569–11579. [[CrossRef](#)]
23. Liu, Y.C.; Lan, J.L.; Zhan, B.; Ding, J.; Liu, Y.; Lin, Y.H.; Zhang, B.; Nan, C.W. Thermoelectric performance of Pb-doped BiCuSeO ceramics. *J. Am. Ceram. Soc.* **2013**, *96*, 2710–2713. [[CrossRef](#)]
24. Sun, Y.; Zhang, C.; Cao, C.; Fu, J.; Peng, L. Enhanced thermoelectric performance in BiCuSeO oxyselenides via Zn and S dual-site substitution. *J. Electron. Mater.* **2017**, *46*, 5909–5915. [[CrossRef](#)]
25. Ren, G.-K.; Wang, S.-Y.; Zhu, Y.-C.; Ventura, K.J.; Tan, X.; Xu, W.; Lin, Y.-H.; Yang, J.; Nan, C.-W. Enhancing thermoelectric performance in hierarchically structured BiCuSeO by increasing bond covalency and weakening carrier-phonon coupling. *Energy Environ. Sci.* **2017**, *10*, 1590–1599. [[CrossRef](#)]
26. Liang, X.; Xu, R.; Kong, M.; Wan, H.; Bai, W.; Dong, D.; Li, Q.; Xu, H.; Li, Z.; Ge, B.; et al. Raising the thermoelectric performance in Pb/In-codoped BiCuSeO by alleviating the contradiction between carrier mobility and lattice thermal conductivity. *Mater. Today Phys.* **2023**, *34*, 101084. [[CrossRef](#)]
27. Liu, Y.; Zhao, L.D.; Zhu, Y.; Liu, Y.; Li, F.; Yu, M.; Liu, D.B.; Xu, W.; Lin, Y.H.; Nan, C.W. Synergistically optimizing electrical and thermal transport performance of BiCuSeO via a dual-doping approach. *Adv. Energy Mater.* **2016**, *6*, 1502423. [[CrossRef](#)]
28. Guo, D.L.; Hu, C.G.; Xi, Y.; Zhang, K. Strain effects to optimize thermoelectric performance of doped Bi<sub>2</sub>O<sub>2</sub>Se via tran-blaha modified becke-johnson density functional theory. *J. Phys. Chem. C* **2013**, *117*, 21597–21602. [[CrossRef](#)]
29. Samourganidis, G.; Kyratsi, T. Continuous and Intermittent Planetary Ball Milling Effects on the Alloying of a Bismuth Antimony Telluride Powder Mixture. *Inorganics* **2023**, *11*, 221. [[CrossRef](#)]
30. Nandihalli, N.; Gregory, D.H.; Mori, T. Energy-Saving Pathways for Thermoelectric Nanomaterial Synthesis: Hydrothermal/Solvothermal, Microwave-Assisted, Solution-Based, and Powder Processing. *Adv. Sci.* **2022**, *9*, 2106052. [[CrossRef](#)]
31. Sun, Y.; Zhang, C.; Cao, C.; Fu, J.; Peng, L. Co-doping for significantly improved thermoelectric figure of merit in p-type Bi<sub>1-2x</sub>Mg<sub>x</sub>Pb<sub>x</sub>CuSeO oxyselenides. *Ceram. Int.* **2017**, *43*, 17186–17193. [[CrossRef](#)]
32. Hsiao, C.-L.; Qi, X. The oxidation states of elements in pure and Ca-doped BiCuSeO thermoelectric oxides. *Acta Mater.* **2016**, *102*, 88–96. [[CrossRef](#)]
33. Lei, J.; Guan, W.; Zhang, D.; Ma, Z.; Yang, X.; Wang, C.; Wang, Y. Isoelectronic indium doping for thermoelectric enhancements in BiCuSeO. *Appl. Surf. Sci.* **2019**, *473*, 985–991. [[CrossRef](#)]
34. Kim, D.; Hong, H.; Lee, J.; Park, S.; Park, K.W. Crystal structure and thermoelectric transport performance of Cu-deficient BiCuSeO oxyselenides. *J. Mater. Res. Technol.* **2020**, *9*, 16202–16213. [[CrossRef](#)]
35. Chen, C.; Delorme, F.; Schoenstein, F.; Zaghrioui, M.; Flahaut, D.; Allouche, J.; Giovannelli, F. Synthesis; sintering, and thermoelectric performance of Co<sub>1-x</sub>M<sub>x</sub>O (M = Na, 0 ≤ x ≤ 0.07; M = Ag, 0 ≤ x ≤ 0.05). *J. Eur. Ceram. Soc.* **2019**, *39*, 346–351. [[CrossRef](#)]
36. Zhang, B.; Hou, Z.; Guo, X.; Du, X.; Gao, Y.; Zhu, Y. Microsized Sn as advanced anodes in glyme-based electrolyte for Na-Ion batteries. *Adv. Mater.* **2016**, *28*, 9824–9830. [[CrossRef](#)] [[PubMed](#)]
37. Li, C.; Guo, D.; Li, K.; Shao, B.; Sun, J. Remarkable enhancement in thermoelectric performance of BiCuSeO through biaxial strain modulation. *Phys. E Low-Dimens. Syst. Nanostructures* **2018**, *97*, 392–400. [[CrossRef](#)]

38. Zhu, H.; Su, T.; Li, H.; Qiang, H.; Hu, M. Thermoelectric performance of BiCuSeO doped with Pb. *Solid State Commun.* **2018**, *278*, 1–5. [[CrossRef](#)]
39. Kim, H.S.; Gibbs, Z.M.; Tang, Y.; Wang, H.; Snyder, G.J. Characterization of Lorenz number with Seebeck coefficient measurement. *APL Mater.* **2015**, *3*, 041506. [[CrossRef](#)]

**Disclaimer/Publisher's Note:** The statements, opinions and data contained in all publications are solely those of the individual author(s) and contributor(s) and not of MDPI and/or the editor(s). MDPI and/or the editor(s) disclaim responsibility for any injury to people or property resulting from any ideas, methods, instructions or products referred to in the content.